

URTeC: 1922872

## Effect of Mineralogy on NMR, Sonic, and Resistivity: A Case Study of the Monterey Formation.

Saul Rivera<sup>1b</sup>, Milad Saidian<sup>1</sup>, Lemuel J. Godinez<sup>1</sup>, Manika Prasad<sup>1</sup>  
1. Colorado School of Mines, <sup>b</sup>Currently at Chesapeake Energy

Copyright 2014, Unconventional Resources Technology Conference (URTeC) DOI 10.15530/urtec-2014-1922872

This paper was prepared for presentation at the Unconventional Resources Technology Conference held in Denver, Colorado, USA, 25-27 August 2014.

The URTeC Technical Program Committee accepted this presentation on the basis of information contained in an abstract submitted by the author(s). The contents of this paper have not been reviewed by URTeC and URTeC does not warrant the accuracy, reliability, or timeliness of any information herein. All information is the responsibility of, and, is subject to corrections by the author(s). Any person or entity that relies on any information obtained from this paper does so at their own risk. The information herein does not necessarily reflect any position of URTeC. Any reproduction, distribution, or storage of any part of this paper without the written consent of URTeC is prohibited.

### Abstract

The Monterey formation has a wide variety of lithologies (diatomites and diagenetically derived cherts, porcelanite, organic-rich mudstones, phosphatic, and carbonate rocks) representing the effect of tectonic, oceanographic, and climatic events. Although the formation has been studied extensively, the effects of lithology on saturation and pore size distributions are still poorly understood. This lack of understanding stems partly from a paucity of data and partly because models built for conventional siliciclastic reservoirs are not applicable. In this study we investigate the differences between biogenic and detrital silica as well as effects of additional influx of clay and carbonate material in the biogenic lithology. Recognizing such differences can help better analyze and interpret NMR, sonic, porosity, and resistivity logs. Our combined laboratory and well log data analysis shows how mineralogy and clay content affect velocities and pore size distributions:

1. With increasing carbonate content, P- and S-wave velocities ( $V_p$ ,  $V_s$ , respectively) increase as compared to silicate-rich rocks.
2. Mineralogical surface relaxivity variations are evaluated by combining mercury intrusion and low-field Nuclear Magnetic Resonance (NMR) data.
3. Considerable amount of porosity is trapped in small pores in the biogenic quartz phase rocks.
4. Pore size distributions in carbonate- or dolomite-rich rocks are distinct from siliceous rocks, and correlate well with higher (above 35%) oil/water ratios.
5. High detrital clay content identified by high Thorium content in spectral gamma ray logs masks the resistivity response due to an increase in neutron porosity (NPHI) and decrease in resistivity.

### 1. Introduction

Siliceous deposits can be described as fine grained silica-rich sediments and sedimentary rocks, which include chert, siliceous shale, and diatomites. Some of the primary minerals that make up siliceous deposits are amorphous silica (Opal-A), cristoballite (Opal-CT), tridymite, chalcedonic quartz, microquartz, and the various combinations of these phases. The source of silica in these sediments is most commonly opaline biogenic debris, such as radiolarians, silicoflagellates, and diatoms. The test and frustules of these marine organisms accumulate in great quantities over extensive areas of the sea floor. Siliceous deposits are most common in polar-regions, the equatorial belt, and other areas of upwelling cold nutrient-rich waters, such as offshore California, North Africa, and Peru (Tada and Lijima, 1983). The unique characteristics of present-day Monterey Formation reflect a combination of the climatic, tectonic, and oceanographic events that formed. It has vast amounts of diatomites and diagenetically derived cherts, porcelanite, as well as organic-rich mudstones, phosphatic, and carbonate rocks (Figure 1).

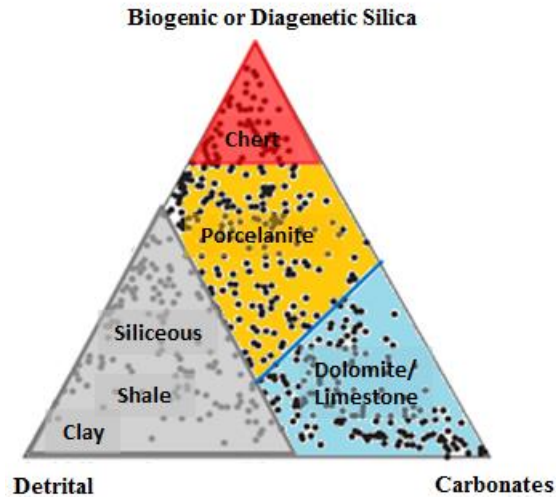


Figure 1: Sedimentary composition range in the Monterey formation. It has vast amounts of diatomites, and diagenetically derived cherts, porcelanites, as well as organic-rich mudstones, phosphatic, and carbonate rocks (Modified from Issacs, 1999 and Schwalbach, 2009).

The Monterey formation is the primary source rock in California, it is also the reservoir for many oil fields such as Kern River, Elk Hills, and Midway-Sunset (Behl, 1999) and has been studied extensively (Blake et al. 1978; Ingle, 1981; Barron, 1986a). Recent reports of recoverable oil (for example, the United States Energy Information Agency, EIA report, 2011) have reignited interest in the Monterey Formation. The EIA (2011) estimates the Monterey/Santos formation as having 15.42 BBO (Billion Barrels of technically recoverable Oil). This is about 4-5 times bigger than the estimates for the Bakken and the Eagle Ford formations (estimated at 3.6 and 3.4 BBO, respectively). Although the Monterey formation does not have continuous areal extent (Figure 2) it, does have a great thickness (1,000 to 3,000 ft) with considerable organic richness (average 2 - 5% by weight, locally as high as 23%) (Behl, 1999).

The Monterey formation contains unique reservoir rocks and complexity due to fractures. A majority of the rocks contain a high proportion of biogenic silica derived from diatoms (Behl, 1999). The diatomaceous rocks are deposited as Opal-A (amorphous silica) that transforms into Opal-CT (critobalite-tridymite) and quartz with increasing burial depth and temperature. Some of the primary reservoir rocks are porcelanites, cherts, siliceous shales, and dolomites. The strata are thinly-bedded, heterogeneous, fractured, and overall difficult to adequately describe and analyze using standard reservoir characterization techniques (Schwalbach et al. 2009). Figure 3 shows an example of lithology and fracture variations of the Monterey formation in an outcrop at Arroyo Burro beach in California.

Despite these extensive, studies, the effects of lithology on saturation and pore size distributions and fracture complexities on reservoir quality are still poorly understood. Understanding reservoir properties of biogenic silicates coupled with recent studies in shale reservoir developments can give the Monterey formation great reservoir potential and aid in its successful development.

The deeper quartz phase rocks have been speculated to have the potential for commercial hydrocarbon production. However, a major cause for limited exploration success is the lack of a systematic study of, as well as a paucity of data on the physical properties of the Monterey formation lithologies. We address this gap by studying the quartz phase of the Monterey formation. Our approach focuses on using laboratory and log data to investigate pore size distributions and porosity-velocity trends considering the effect of mineralogy. The methods for this investigation include laboratory nuclear magnetic resonance (NMR) and ultrasonic measurements as well as log data. We present here our data and interpretations, as well as correlations between well logs and laboratory data in order to better quantify the pore space and examine the controls these factors exert on reservoir performance.

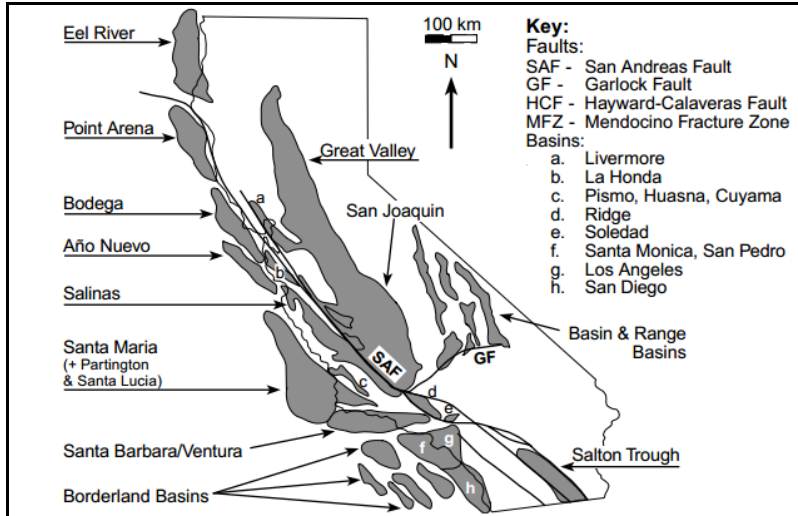


Figure 2: Present location of Neogene sedimentary depocenters in California. The figure shows the continuous nature of the depocenter and local tectonic. Monterey formation does not have continuous areal extent (Behl, 1999).



Figure 3: Example of different types of fracturing in the Monterey formation at Arroyo Burro Beach. The strata are thinly-bedded, heterogeneous, fractured, and overall difficult to adequately describe and analyze using standard reservoir characterization techniques.

## 2. Sample Set

The available log and core data for this study covers the Gould, Devilwater, McDonald, and Antelope Members of the Monterey formation. We studied a total of 19 core samples from the Gould, Devil Water, McLure, and Antelope members of the Monterey formation and depths varying from 5000 to 9000 ft. The mineralogy data were acquired by a commercial vendor. X-Ray Diffraction Data (XRD) was not available for some of the exact samples studied here. However, XRD data was available for cores in close proximity to the samples used (for example core 7220.8', 7226.3', and 8154.5') (Table 1). We checked the applicability of the XRD measurements for samples taken within the same interval as the XRD data by comparing core photos of the entire cross section with the available core samples. The samples were picked to represent a wide range of lithologies. For example, the core sample at 5360' has a quartz content of 83.6% quartz, while sample 8539' is 91.5% dolomite. There is also a variation in the clay content, the minimum clay content was 0% (sample 8539') and the maximum was 41.8% (sample 8288').

Table 1: Conventional core x-ray diffraction for samples used in this study, the samples represent a wide range of lithologies that can be found in the lower section of the Monterey formation. NA represents not available data.

Core Depth (ft)	Analyzed Core Depth (ft)	Quartz (Weight %)	Plagioclase (Weight %)	K-Feldspar (Weight %)	Calcite (Weight %)	Fe/Mg-Dolomite (Weight %)	Siderite (Weight %)	Pyrite (Weight %)	Total Clay (Weight %)
5360	5360	83.6	0.7	1.6	2.8	1.5	0	2.6	7.3
5440	5440	55.2	0.5	0	0	38.5	0	1.0	4.9
7223.7	NA	NA							
7226.3	7225.00	67.0	2.0	4.0	8.0	3		7.0	9
7228.2	NA	NA							
7720.8	7720.75	69.0	6.0	4.0	4.0	5		3.0	10
7750.8	NA	NA							
7751.8	NA	NA							
7906	7906	59.2	1.8	4.1	15.5	4.0	0	4.3	11.1
8154.5	8154.15	68	6	5	9.0	4		1	7
8272	8272	NA							
8288	8288	39.0	3.2	5.9	0	2.9	1.2	5.9	41.8
8333	8333	77.5	1.3	2.2	8.8	1.6	0	1.7	6.8
8539	8539	8.1	0	0	0	91.5	0	0.4	0
8632.2	8632.2	50.4	5.2	3.3	6.9	1.4	3.3	5.4	24.2
8935.1	8935.1	77.0	1.8	2.5	6.1	1.3	0.7	2.1	8.4
9097	9097	71.0	3.3	1.4	9.9	2.3	1.6	2.0	8.5
9193	9193	72.6	3.6	2.2	0	2.5	0.6	3.7	14.7
9447.5	9447.5	10.6	0	0	0	82.7	0	1.1	5.6

Porosity, permeability, and saturation data from a commercial vendor was also available (Table 2). For several core samples the data does not correspond to the cores available. As before, data from samples that were in close proximity was used.

Table 2: Porosity, permeability, and saturation data available for samples used in study. F/ implies visible fracture on the core sample.

Core Depth	Core Depth Used for Analysis	Permeability		Porosity	Fluid Saturation			Grain Density
		$K_{air}$			Oil	Water	O/W	
ft	ft	Fracture	md	p.u.	%	%	Ratio	$g/cm^3$
5440.0	5440.0	F/	4.39	12.82	15.75	72.09	0.22	2.52
7223.7	7224.0		1.61	2.80	31.70	68.10	0.47	2.50
7226.3	7226.1	F/	3.33	3.20	40.50	58.80	0.69	2.51
7228.2	7228.1		0.25	6.00	48.10	40.00	1.20	2.54
7720.8	7720.8		0.31	5.40	43.80	55.90	0.78	2.52
7750.8	7751.0		0.02	4.50	37.00	61.20	0.60	2.50
7751.8	7751.8		1.08	20.00	60.20	23.70	2.54	2.75
7906.0	7906.0	F/	4.34	5.56	30.72	60.30	0.51	2.59
8154.5	8154.3		0.02	1.60	38.90	40.30	1.46	2.52
8288.0	8288.0	F/	3.37	5.79	31.15	53.00	0.59	2.45
8333.2	8333.2		0.11	1.96	11.55	86.43	0.13	2.54

8539.0	8539.0		0.07	1.52	9.42	16.58	0.57	2.84
8632.2	8632.2		0.03	1.70	6.80	89.30	0.08	2.52
9097.1	9097.1		0.01	1.01	22.86	60.36	0.38	2.55
9193.1	9193.1		0.01	2.14	10.99	87.04	0.13	2.58
9447.5	9447.5		0.04	1.02	22.68	59.88	0.38	2.84

### 3. Methodology

#### 3.1 Ultrasonic Measurement

Ultrasonic velocity measurements were performed using a pulse transmission method both at benchtop and under confining pressure. In this method, a pulse generator generates electrical pulses that are converted by a piezoelectric transducer into elastic waves. The wave then travel through the core sample and the signal is received on the opposite end by another transducer. The receiver transducer transforms the elastic wave into an electric pulse that is then recorded by a digital oscilloscope. The wave is recorded from the oscilloscope and the velocity and other signal attributes are calculated.

Figure 4 for benchtop measurements shows how the transducers are placed directly on the core using an acoustic couplant (from Sharma et al., 2013). The direction in which the transducers are applied depends on the direction of the laminations. The main purpose for the benchtop measurements is to identify the directions of minimum and maximum velocity for transducer alignments under pressure.

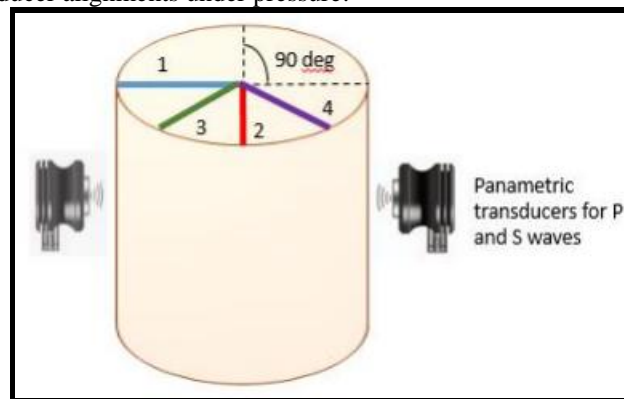


Figure 4: Core assembly for benchtop measurements. Colored lines represent the different directions in which the measurements were taken.

Seven samples were prepared for pressurized measurements. The samples were prepared for ultrasonic measurements as well as conductivity measurements, however the conductivity measurements will be part of future studies in which the anisotropy from ultrasonic and resistivity measurements will be analyzed. There were two factors taken into consideration for the placement of ultrasonic crystals for velocity measurements under pressure. The first is the direction of the laminations of the samples. This is taken into account in order to understand the wave propagation and polarization. The second is that in order to account for anisotropy of the rock sample, the ultrasonic crystals need to be placed at  $0^\circ$  and  $90^\circ$  directions. These angles constitute the naming convention of the velocities, where  $V_{p90}$  denotes a measurement performed in the direction perpendicular to the direction with the highest recorded velocity (called  $V_p^0$ ) obtained during the benchtop measurements. Based on these factors, a decision is made on the optimum placement of the ultrasonic crystals, surfaces were made flat by filling down the sides (Figure 5a). This was done in order to obtain a good connection between the crystals and the core. The crystals used in this experiment were obtained from Piezo-Optics and they have a frequency range of 50 KHz to 100 MHz (+/- 5%). Each one of the crystal pieces has to be prepared. The first step preparing the crystal is to cover all the sides where the piezoceramic (quartz) is exposed. Next the end of an insulated wire is cleaned and glued to the electrode surface of the crystal with silver conducting epoxy. Once the conducting epoxy is dried 5 minute epoxy is added on top. The next step in the preparation is to place the crystals on their respective places, which first involves spreading silver conducting epoxy on the flat areas and in the spaces in-between them (Figure 5b). It is important to press on the crystals when they are first placed in order to get rid of any air bubbles. The next step is to test and record signals in

the sample. If the signals are satisfactory the end caps are glued to the end surfaces using K-20 epoxy (Figure 5c). Finally, the exposed surfaces (sides) of the sample are covered in a flexible epoxy jacket. For this experiment it was decided to use EP1121 epoxy (Resin lab). The velocity was measured during pressure loading and unloading. Additionally, the signals were recorded using 10 us/div and 4 or 2 us/div.

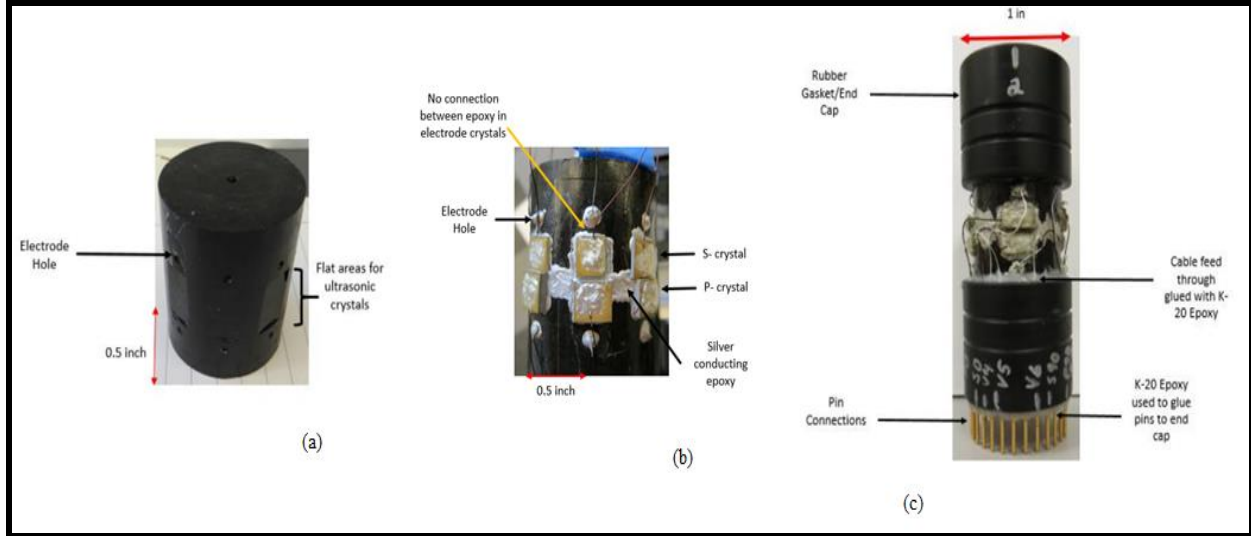


Figure 5: Core assembly process for pressurized measurements. (a) Core sample after electrode holes have been drilled and surfaces have been made flat for ultrasonic crystals. (b) Core sample with ultrasonic crystals (P and S) and electrodes on their respective places. Notice that there is no connection between the crystals as this could cause shorting. Additionally, there is no connection between the silver epoxy use to connect the crystals and the resistivity electrodes. (c) End caps are glued to the ends of the core and individual cables are passed through the feed throughs in the end caps.

In order to compare ultrasonic measurements with sonic logs, several factors must be taken into account. First, the frequency for ultrasonic measurements is about 0.5 MHz or more, while for sonic frequency is in the range of 10 kHz. The measurements of samples at benchtop conditions will not show the effect of pressure while the logging data will show the effect of pressure. We will investigate the effect of pressure on the cores with measurements performed at pressurized measurements. Second, the ultrasonic measurements were performed on dry samples and sonic logging data shows the effect of fluid saturation. The dry rock velocities can be converted to saturated rock data using Gassmann fluid substitution (Gassmann, 1951). The data from the dry samples are mathematically saturated by using P-wave ( $M$ ) modulus approximation provided by Mavko et al. (1995). This method is based on the fact that the bulk modulus in Gassmann's relationship can be replaced by the  $M$ -modulus. The equation for  $M$ -modulus is as follows:

$$M_{\text{dry}} = \rho V_P^2 \quad (\text{Mavko et al. (1995)})$$

where  $\rho$  is the grain density in  $\text{g/cm}^3$ , and  $V_P^2$  is the compressional velocity in  $(\text{km/s})^2$ .

The equation used to calculate the  $M$ -modulus is as follows:

$$M_{\text{sat}} = (M_s) * \left( \frac{\phi M_{\text{dry}} - \frac{(1 + \phi) K_f M_{\text{dry}} + K_f}{M_s}}{(1 - \phi) K_f + \phi M_s - \frac{K_f M_{\text{dry}}}{M_s}} \right) \quad (\text{Chaika, 1998})$$

where  $M_{\text{sat}}$  and  $M_s$  (calculated using Voigt, Reuss, and Hill average) are the saturated solid  $M$ -modulus, respectively.  $K_f$  is bulk density of fluid, in this case brine.

### 3.2 NMR measurements

We used a Magritek™ 2MHz core analyzer to measure the transverse relaxation time ( $T_2$ ). The  $T_2$  relaxation time is a result of a mathematical inversion of the decay time. NMR and  $T_2$  responses are based on different fluid types and

properties of the porous material such as pore size distribution and wettability (for more information see Coates et al. 1999). As mentioned earlier, for this study we will only concentrate on the pore size distribution of the rocks as the wettability may have been compromised as the cores were cleaned by different chemicals.

For this experiment two data acquisitions were made. The first acquisition was done after the sample parameters such as length, diameter, and weight had been measured, and the samples had been oven-dried at 60 °C. These measurements were used to mainly identify clay minerals. While clay-poor samples would not give useful data, since clays retain water even at high temperatures, NMR experiments of dry samples allow us to identify any clay bound water volume. The problem with this type of experiment is that in the processes of obtaining the NMR signal the sample is exposed to the atmosphere and depending on the humidity conditions in the lab, hydrogen can be adsorbed from the atmosphere. Another problem is that even clay-rich but dry samples have a very weak signal and the background noise can mask any type of information that can be obtained. This means that distributions that might seem properties of the rock could actually end up being background noise. In order to help alleviate this problem a background correction using an empty probe was made.

For the second set of experiments, the cores were saturated using a brine solution. The brine salinity (20,000 ppm) matched the average salinity determined from different formation fluid tests. The samples were saturated for a total of two weeks under 600 psi pressure. After saturation, NMR signals were obtained for each sample. The acquisition parameters for the measurements include number of scans, pulse length, number of echoes, and echo time. A background signal is also obtained after this set of experiments as the laboratory conditions might have changed during the period of saturation of the cores.

The next step was to run an NMR experiment on the bulk fluid. A critical aspect of this step is to ensure that the volume of fluid used to obtain the signal is known with a good precision. In this case, 25 ml (of the 20,000 ppm salinity brine) was measured using a pycnometer at normal laboratory conditions. In the NMR experiment, the initial amplitude of the raw decay curve can be directly proportional to the number of hydrogen nuclei that have been polarized in the pores. Therefore, the amplitude can be calibrated to porosity by using the NMR signal from the known volume of the bulk fluid.

## 4. Results and Discussion

### 4.1 Ultrasonic Velocity

In order for seismic interpretation to be performed correctly, the velocity-porosity trends and velocity anisotropy understanding is critical. The first step in understanding the trends is to investigate porosity-velocity trends for these siliceous non-granular rocks. Most of the samples in the Monterey formation contain laminations or fractures that affect velocity values. Generally, it has been found that mudstones of source-rock reservoirs can but need not be anisotropic in the lamination scale of millimeters, the scale of core samples. However, they are always anisotropic in the bed scale of centimeters to meters (Hart et al. 2013). It will be important to establish if anisotropy will be a factor in the Monterey formation at each scale, whether it is core or bed scale. Any porosity inversions from seismic and well log data will need to account for velocity anisotropy. Additionally, analyzing the pressure dependence in the samples will be critical to understand the applicability of the measurements to downhole conditions.

Figure 6 shows an example of the wave forms obtained at benchtop conditions. Although plots were made for each sample, only one representative sample is presented here. Figure 6 shows the compressional wave propagation for sample 7906 in four different directions. This sample shows a significant change in velocity between  $V_{p0}$  and  $V_{p90}$ . As it can be seen from the optical image in Figure 6 the sample has significant bedding fractures some of which are calcite filled.

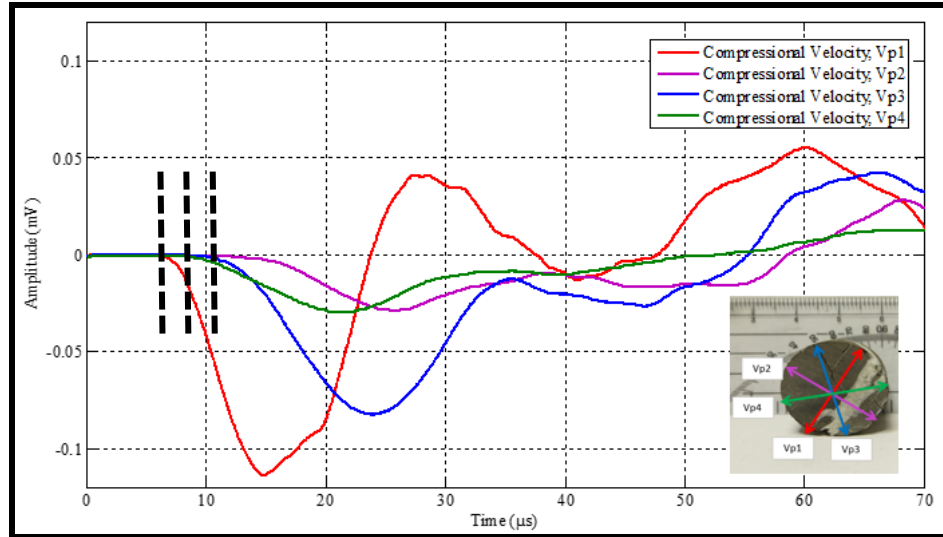


Figure 6: Compressional wave propagation along four different directions for sample 7906. Picture of core is included to show the different directions. This sample shows significant change in velocity between the  $V_{p0}$  and  $V_{p90}$ . As it can be seen from the optical image the sample has significant bedding fractures some of which are calcite filled. Dashed lines mark the arrival times.

Table 3 gives a summary of the compressional velocities along different directions for all of the samples. As it can be observed from Table 3,  $V_{p0}$  or the compressional velocity in the parallel direction has higher velocity values than  $V_{p90}$  which is the perpendicular direction, which correlations with the direction of observed laminations. Additionally, the  $V_{p45}$  and  $V_{p135}$  velocities lie in between the  $V_{p90}$  (minimum) and  $V_{p0}$  (maximum). The only exception is sample 8288 which has a  $V_{p90}$  that is almost 4 times bigger than  $V_{p0}$ . The velocity in the  $45^\circ$  degrees direction lies between the  $0^\circ$  and  $90^\circ$ . This type of velocity information at different degrees can be very helpful can working on transversely anisotropic models for mechanical properties as they will allow for calculation of the stiffness tensor and calibration with sonic logs.

Table 3: Summary of compressional velocities obtained for core samples.  $V_{p0}$  was measured parallel and  $V_{p90}$  perpendicular to any aligned textures. The velocities were obtained at benchtop conditions.

Depth (ft)	Compressional Velocity, $V_{p0}$ (km/s)	Compressional Velocity, $V_{p45}$ (km/s)	Compressional Velocity, $V_{p90}$ (km/s)	Compressional Velocity, $V_{p135}$ (km/s)	Average Compressional Velocity, $V_{p_{ave}}$ (km/s)
5360	4.00	3.56	3.13	3.21	3.47
5440	3.44	3.43	3.38	3.44	3.42
7906	3.89	3.04	3.01	3.02	3.24
8288	1.07	1.59	4.16	1.46	2.07
8539	6.15	5.93	5.76	5.26	5.78
8632	4.63	4.12	3.33	3.93	4.00
8935	4.82	4.78	4.70	4.72	4.76
9097	5.05	4.90	4.98	4.80	4.93
9193	4.62	4.48	4.32	4.47	4.47
9447.5	6.23	6.20	6.09	6.22	6.18

For pressurized ultrasonic measurements, compressional and shear wave propagation at  $0^\circ$  and  $90^\circ$  (i.e. parallel and perpendicular to any textures such as, bedding, microfractures) were obtained. Figure 7 shows an example of the

compressional and shear wave propagations at different pressures for sample 7228.2. The waveforms for the  $0^\circ$  and  $80^\circ$  direction are shown. The difference in compressional wave velocity between  $V_{p0}$  and  $V_{p90}$  is about 0.12 km/s, while a difference between  $V_{s_0}$  and  $V_{s_{90}}$  is about 0.6 km/s.

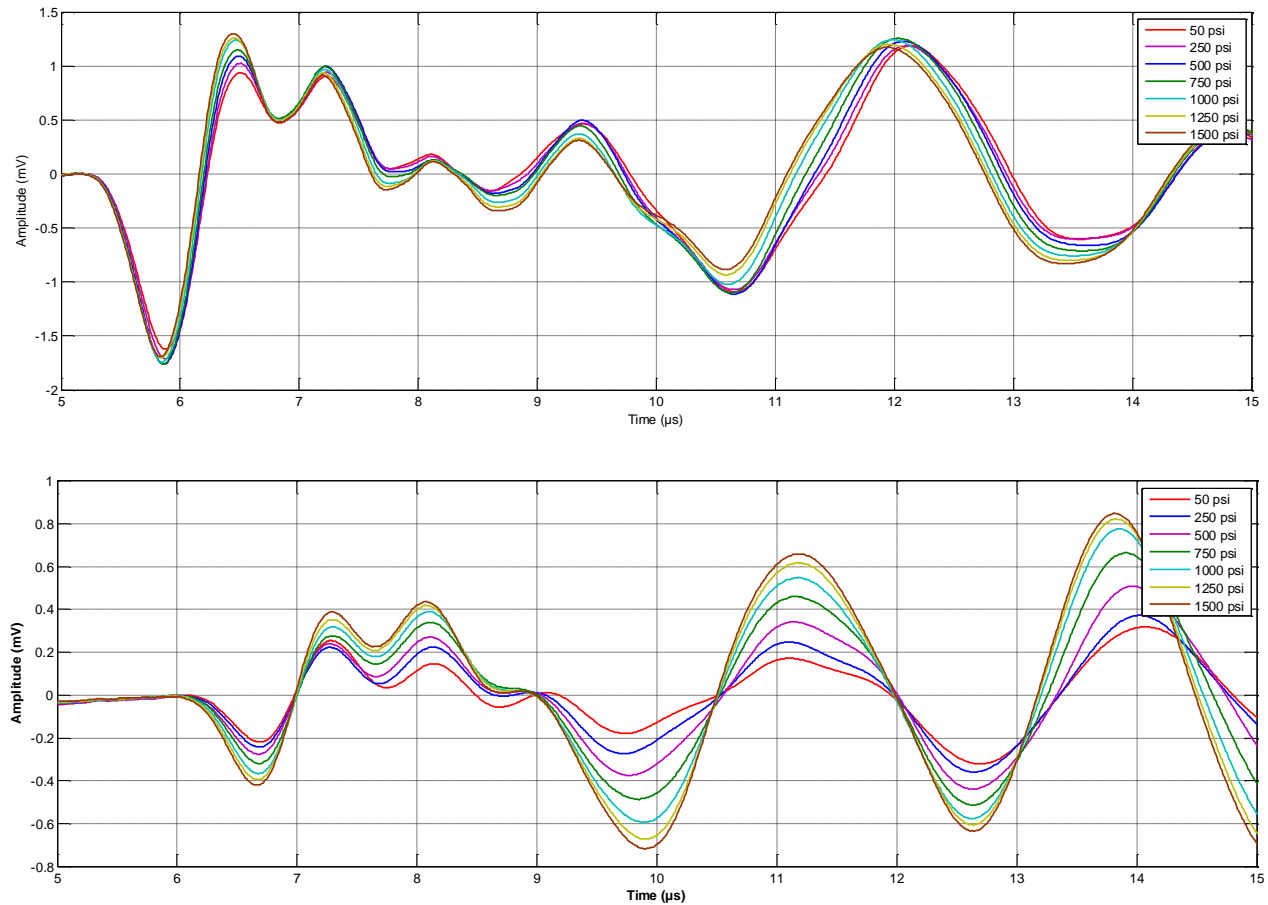


Figure 8: Example of compressional wave propagation at varying pressures for sample 7223.7 at  $0^\circ$  and  $90^\circ$ . The figure shows the anisotropy in the sample and the low pressure dependence. Each color denotes a different pressure step.

Using travel time data obtained from graphs such as that shown in Figure 8, velocities values were calculated for each pressure step. Table 4 gives a summary of only the  $V_{p0}$  and  $V_{p90}$  values for each sample at 1,000 psi during the pressure loading and unloading. Also note that Figure 8 does not show much pressure dependence. CT-scans of various samples reveal that although the core samples contain micro-fractures. Some of the fractures have been filled with higher density material (most likely calcite) which would not compress as much and would show less pressure dependence than if they fractures were not filled. Additionally, since the samples do not show much pressure dependence it opens the possibility in the future to just obtain velocity measurements at benchtop conditions. However, this must be done with caution.

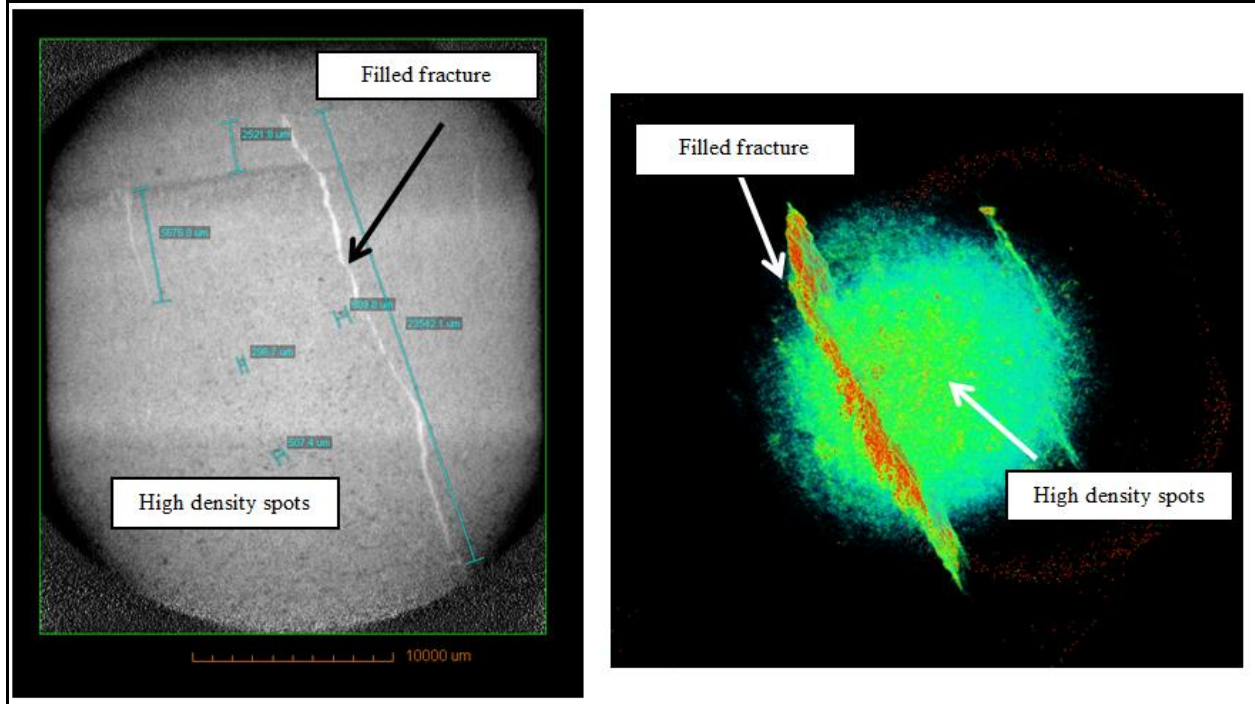


Figure 9: CT-Scan of Monterey sample showing filled micro-fractures and sections with high density material (most likely calcite). It shows that samples contain microfractures which can act as conduit for hydrocarbon flow as well as decrease the pressure dependence on the rocks and increase the velocity values.

Table 4: Summary of  $V_{S0}$ ,  $V_{p90}$ ,  $V_{S0}$ ,  $V_{S90}$  velocities obtained for core samples. The velocities were obtained at a confining pressure of 1000 psi.

Sample	Cycle	Compressional Velocity (km/s)		Shear Velocity (km/s)		Velocity Ratio (unitless)	
		$V_{p0}$	$V_{p90}$	$V_{S0}$	$V_{S90}$	$V_{p0}/V_{S0}$	$V_{p90}/V_{S90}$
7223.7	Loading	4.82	4.7	3.1	3.04	1.55	1.55
7223.7	Unloading	4.78	4.73	3.05	3.01	1.56	1.57
7228.2	Loading	4.81	4.01	3.03	2.56	1.59	1.56
7228.2	Unloading	4.83	4.17	3.02	2.61	1.6	1.6
7626.3	Loading	4.6	4.5	3.05	2.95	1.51	1.53
7626.3	Unloading	4.64	4.55	3.05	2.94	1.52	1.55
7750.7	Loading	4.14	NA	2.28	2.24	1.81	NA
7750.7	Unloading	4.11	NA	2.24	2.24	1.83	NA
7751.8	Loading	4.72	4.4	2.72	2.72	1.73	1.62
7751.8	Unloading	4.76	4.42	2.73	2.7	1.75	1.64

Very few studies exist about the velocity variations in biogenic silicate reservoirs such as the Monterey formation. However, Chaika (1998) obtained ultrasonic measurements from samples in the Monterey formation from three different fields in the San Joaquin Basin such as Cymric, McKittrick, and Asphalt. The cores from Cymric Field consists mainly of Opal-A and Opal-CT. The data from McKittrick Field consists mainly of Opal-CT (65% to 97%)

by weight and the Asphalt is mainly composed of quartz (36% to 70%) by weight. The cores obtained from this study lie in close proximity to the Midway-Sunset field which lies along the same depositional trend as Chaika's (1998) data. Thus, the Opal data from Chaika (1998) can be extended with the porcelanite and quartz data obtained in this study. Figure 10a shows the compressional velocity-porosity trends, with the velocity being plotted being the average compressional velocity of the 0° and 90° directions. As it can be observed there is a strong inverse relationship between compressional velocity and porosity ( $R^2$  value of 0.91). However, there are a few exceptions that are of particular interest. Some samples (7906, 7751.8, 8539, and 9447.5) deviate from the main velocity-porosity trend, the latter samples have higher velocities while sample 7906 has a lower velocity value than the main trend. The deviations in velocity values are due to the differences in mineralogy. Figure 10b shows the compressional velocities after fluid substitution. As it can be observed the velocities increased after fluid substitution by about 0.5 km/s.

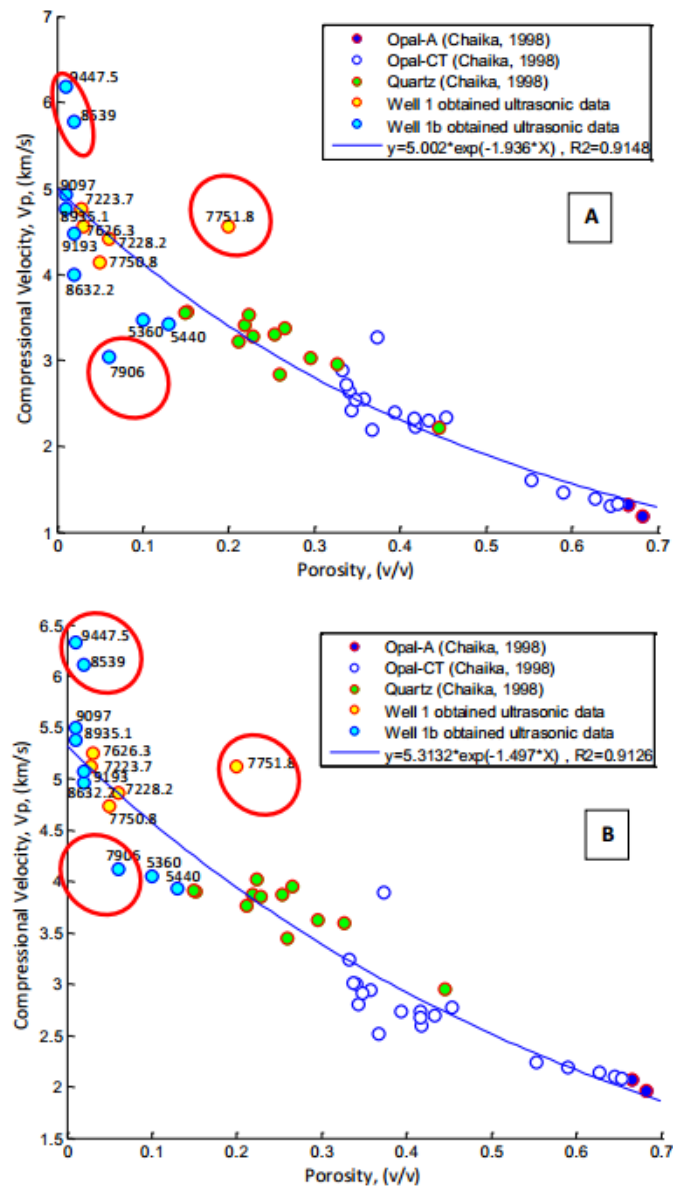


Figure 10: Compressional velocity – porosity trends for data collected in this study along with data collected by Chaika (1998) for Opal-A, Opal-CT, and quartz phase rocks from the San Joaquin Basin. (a) Velocity from dry rock samples. (b) Velocity after fluid substitution.

We discussed the effect of compositional and geological properties of the rock such as mineralogy and diagenesis as well as textural properties such as microfractures and layering on velocity-porosity relationships. In the following section, we take one step further and study the effect of aforementioned properties on pore size distribution NMR measurements.

#### 4.2 NMR Measurements

In the absence of published data on quartz phase rocks from the Monterey formation, assumptions are made that once these rocks have reached the diagenetic stage of quartz, most of the porosity has been lost and they are not be seen as ideal rock types for hydrocarbon storage and production. However, Bohacs et al. (2005) have shown that presence of other minerals such as clays or carbonates can slow these diagenetic changes. The focus of this section is to investigate existence of any pore size distribution variations within the quartz phase rocks from the Monterey formation and their relation to mineral compositions and detect any direct implications to reservoir performance as well as draw conclusions from variations observed in velocity-porosity measurements.

Results from low field NMR measurements are reported to understand the pore size distribution in rocks from the Monterey formation. As mentioned earlier the measurements were performed at dry and saturated conditions. Additionally for each set of measurements (dry and saturated) an experiment was run on the same day of the measurements to record the background noise in the NMR instrument. In the first stage of the NMR measurements, signals for dry samples were obtained to determine if the data can be analyzed to quantify the amount of any bound water present in the samples. The analysis showed that the  $T_2$  distributions for all samples lie between 0.01 and 1 msec, with a median at 0.1 msec. However, after the background correction was performed, the initial distribution centered at 0.1 msec was removed. In the second stage, the NMR was obtained after the samples had been saturated under the conditions described earlier. In addition distributions from 0.01 and 1 msec with a median at 0.1 msec obtained in the dry samples, the saturated samples showed distributions between 1 to 1000 msec. However, after a background correction was applied the distribution centered at 0.01 was removed. Another important aspect to take into consideration is the minimum instrument resolution. For this equipment the minimum instrument time resolution is 0.06 msec. Initially for the dry measurements a significant portion of the raw signal obtained from the dry samples lied below the instrument resolution. However, once the samples were saturated and most importantly, after a background correction was been performed the NMR  $T_2$  distribution below the 0.06 msec diminished and was therefore ignored.

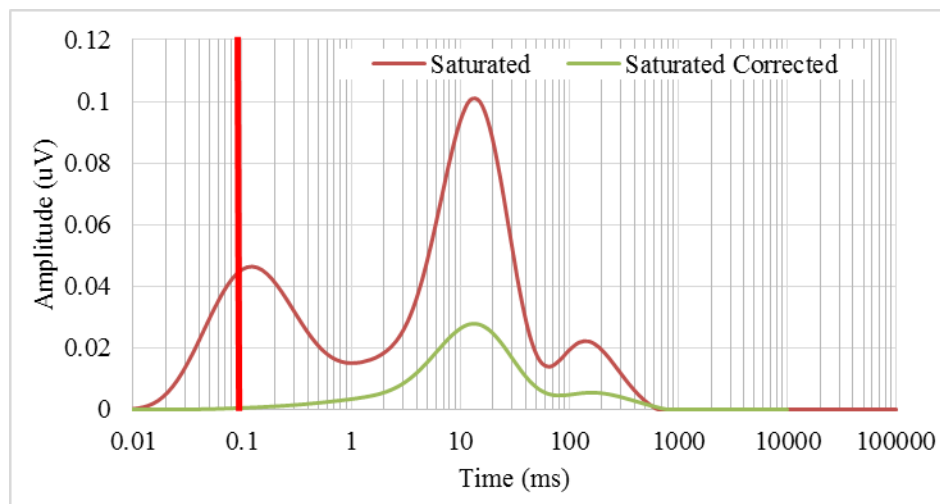


Figure 11: Example of NMR  $T_2$  distribution before and after background correction. Emphasizes the importance of obtaining and performing background correction on signals. Red line at 0.06 usec shows instrument resolution.

#### Quartz Dominated

Figure 12 the  $T_2$  distribution relaxation time distribution obtained from core samples with high quartz content. The figure shows that core samples have similar shape distribution and XRD data for samples 7220.8 and 8154.5 show that they have quartz content higher than 65% (by weight) (Table 1). The main difference lies between samples at

shallow (5000 to 7000 ft) and deeper samples (deeper than 8000 ft). The differences in the distribution can be explained by the fact that cores in the shallower section and have bigger pore sizes as they have not been compacted to the same extent as the rest of the samples. Another explanation is that as mentioned earlier, shallower depths of the Monterey formation correspond to a time of basin filling (Graham and Williams, 1985) which means more clastic input can be expected. Therefore, the differences in incremental porosity distributions can also be attributed to differences between clastic quartz and biogenic quartz. The latter having significant amount of its porosity the micro range. However, sample 8333 does not have the same distribution as the rest of the samples. This is due to the fact that it has a low signal to noise ratio. Sample 54773.3 does not have XRD data available as mentioned earlier however, by the shape of the distribution it can be speculated that its bulk mineralogy is mainly composed of quartz.

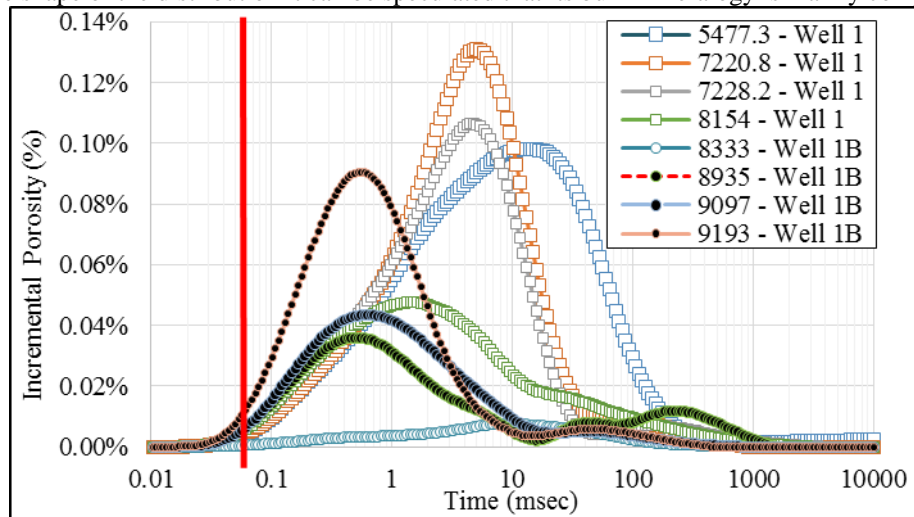


Figure 12: Incremental porosity-time distributions for quartz rich samples at different depth ranges. The cores presented in this graph have similar shape and have quartz content higher than 60%. Red line at 0.06 msec represents the minimum instrument resolution.

### Dolomite Dominated

Figure 13 shows  $T_2$  distributions for two core samples that are dolomite dominated. Samples 8539 and 9447.5 have a dolomite content higher than 80% (Table 1). As opposed to the quartz dominated samples these samples have a clear bimodal distribution. The bimodal distribution can be explained by the fact that even though the samples are mainly composed of dolomite the rest of the composition can be quartz, which would explain the small pore size distribution. An important fact to mention is that the ultrasonic analysis showed that these samples did not follow the trend of silica diagenesis for the Monterey and they also had the highest oil/water ratios. The reason is because the samples have a higher carbonate content which increases the velocities.

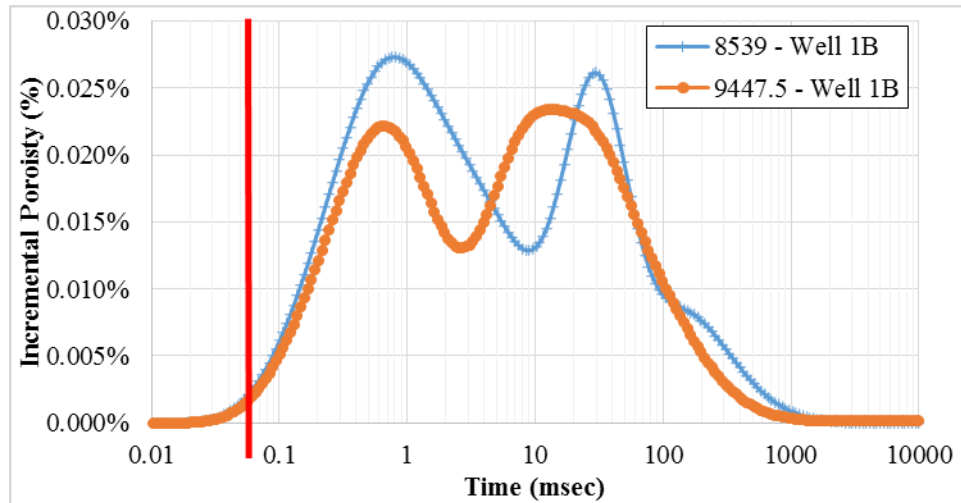


Figure 13: Incremental porosity – time distributions for carbonate rich samples. The cores presented in this graph have similar shape and have dolomite content higher than 80%. Red line at 0.06 msec represents the minimum instrument resolution.

#### High clay/mix of sediments

Figure 14 shows  $T_2$  distribution from NMR samples plotted 8288 and 8632. The bulk mineralogy of sample 8288 is composed of 41.8% total clay, 39% quartz, 5.9% feldspar, and 2.9% dolomite. This sample shows a bimodal distribution with a significantly higher distribution at lower  $T_2$  times. Sample 8632 is composed of 50.4% quartz, 24.2 clays, and 6.9% calcite. The distribution at lower times (0.1 to 1 msec) is less pronounced for this sample however two distinct distributions can be observed at higher times (1 to 11 msec and 11 to 300 msec). The pore size distribution in the for the lower relaxation times can be attributed to clays and small pores in quartz, while the larger pores will be a contribution from carbonates and larger pores in quartz.

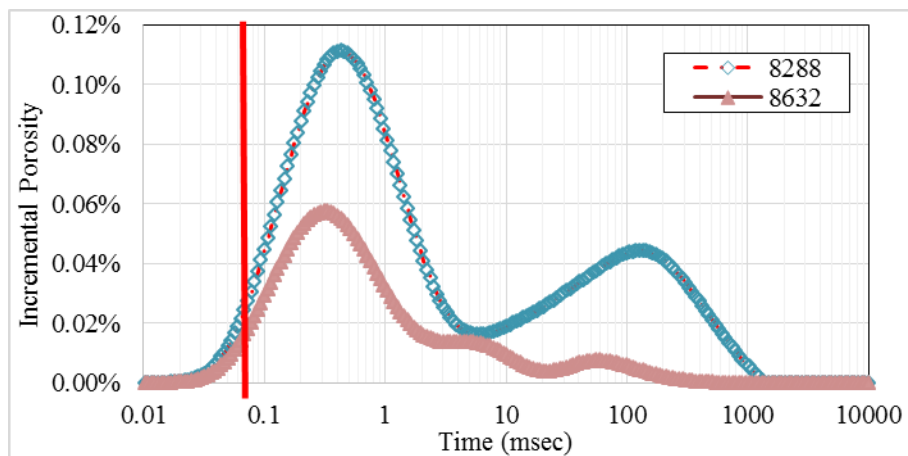


Figure 14: Incremental porosity – time distributions obtained from samples with high clay content. XRD data from these samples shows high clay content and a mix of quartz, feldspar, and dolomite. Red line at 0.06 msec represents the minimum instrument resolution.

Greeney and Godinez (2013) studied the spontaneous imbibition of oil and brine using dielectric microscopy for the same set of samples presented in this study. They showed that the area with carbonate content has some imbibition while the quartz/plagioclase does not. In addition to the mapping of imbibition Greeney and Godinez (2013) obtained QEMSCAN which showed that microfractures have a diverse portion of minerals, but are mainly composed of carbonates as predicted by the CT-scans, velocity behavior, and pore size distributions in this study. This shows that the fractures mentioned earlier not only have an effect on acoustic values and anisotropy of the rock, but also on the pore size distributions and wettability of the rock. It can also help to explain the high velocities and

low pressure dependence where the quartz and dolomite are mixed giving the overall frame of the rock a greater stiffness. Additionally Greeney and Godinez (2013) showed that clay and other minerals are helping to hold brine in some areas. These observations help in the porosity comparison and resistivity analysis; where we will expect the NPHI porosities to be higher and resistivity to be lower for those sections.

Figure 15 shows the velocity-porosity trends and its relationship to NMR  $T_2$  distribution. As it can be seen from the figure, areas that had been identified as a specific lithology also have similar  $T_2$  distributions. Additionally it can be observed that samples that showed deviation from the diagenesis trend have higher carbonate content and that these samples also have higher oil/water ratios and larger pore sizes. This also correlates well with the observations made by Greeney and Godinez (2013) which showed that oil preferentially imbibe sections that have higher carbonate content.

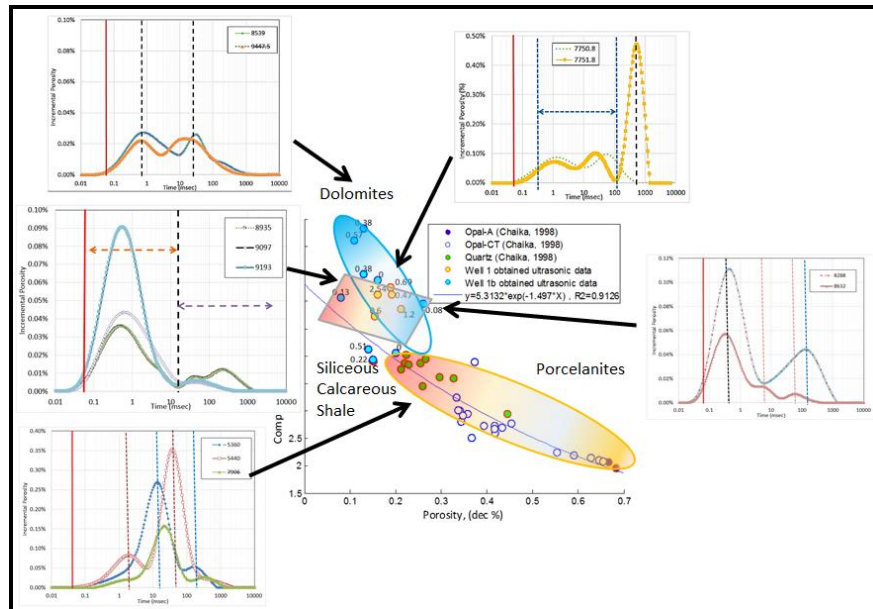


Figure 15: Compressional velocity-porosity trends for data obtained from this study along with data collected by Chaika (1998) for Opal-A, Opal-CT, and quartz phase from the San Joaquin Basin.

#### NMR Porosity Comparison – Influence of Clay

After obtaining the incremental porosity and  $T_2$  relaxation time distributions, the cumulative of the incremental porosities was calculated in order to get an estimation of the total porosity.

Table 5 shows a summary of the calculated NMR porosities for different core samples as well as the density, the neutron, and the helium porosities. The table shows an overall good agreement with the porosity obtained by using helium porosimetry. However, when compared to density and neutron porosity the values are lower by a factor of two. Additionally the NPHI porosity values are considerably higher the rest of the porosities. This can be attributed to the effect of hydrogen bound to the structure of the clays; however this would be further analyzed.

Table 5: Table shows the calculated porosity values from NMR  $T_2$  distributions and comparison to other porosity measurements. NMR porosity shows that it is in good agreement with the porosity obtained from Corelab (helium). However, values deviate from those obtain by CMR tool

and Density Porosity. Additionally, lab NMR and Neutron porosity show the biggest difference, which has been attributed to the to the hydrogen bound in the structure of the clays.

<b>Depth (ft)</b>	<b>Lab NMR Porosity (ml/ml)</b>	<b>Total CMR Porosity (cc/cc)</b>	<b>Helium porosity (v/v)</b>	<b>Density Porosity (v/v)</b>	<b>Neutron Porosity (v/v)</b>
<b>5360</b>	0.11	0.09	0.11	0.15	0.21
<b>5440</b>	0.14	0.08	0.13	0.05	0.15
<b>7906</b>	0.06	0.09	0.06	0.09	0.15
<b>8288</b>	0.07	0.04	0.06	0.08	0.17
<b>8333</b>	0.01	0.04	0.02	0.09	0.14
<b>8539</b>	0.02	0.06	0.02	0	0.11
<b>8632</b>	0.03	0.03	0.02	0.09	0.25
<b>8935</b>	0.02	0.03	0.01	0.08	0.15
<b>9097</b>	0.03	0.03	0.01	0.09	0.13
<b>9193</b>	0.04	0.02	0.02	0	0.08
<b>9447.5</b>	0.02	0.07	0.01	0	0.13

Identification of pay zones with conventional methods, such as identifying high resistivity zones in hydrocarbon-bearing zones is a major problem in exploration of the middle and lower sections of the Monterey formation. Zones with high resistivity values have been found to produce mainly water, while zones with low resistivity have been found to produce profitable amount of oil. With this problem in mind and the observation that NPHI overestimates the porosity values for deeper zones (

Table 5), the next step was to analyze any indication of clay. Figure 16 shows thorium and potassium crossplots with deep resistivity as color scale for two wells (Figure 16A and Figure 16B). Figure 16A and Figure 16B show that an increase in thorium and potassium content is marked by a decrease in the recorded resistivity values. In general, Figure 16B appears to have higher thorium content than Figure 16A. Hassan et al. (1976) have associated the increase in thorium values with increased input of terrigenous clays. Additionally, Bohacs and Schwalbach (1994) reported that for the Monterey formation in Naples Beach California, high levels of thorium occur coincident with volcanic ash beds, while potassium correlates with aluminum which is a predictor of detritus content. Therefore, the increases in potassium and thorium content observed in the lower section of the Monterey can be attributed to increases of input in terrigenous clays and resistivity values. The bound water in the clays would increase the NPHI readings (higher hydrogen content) and reduce the resistivity readings.

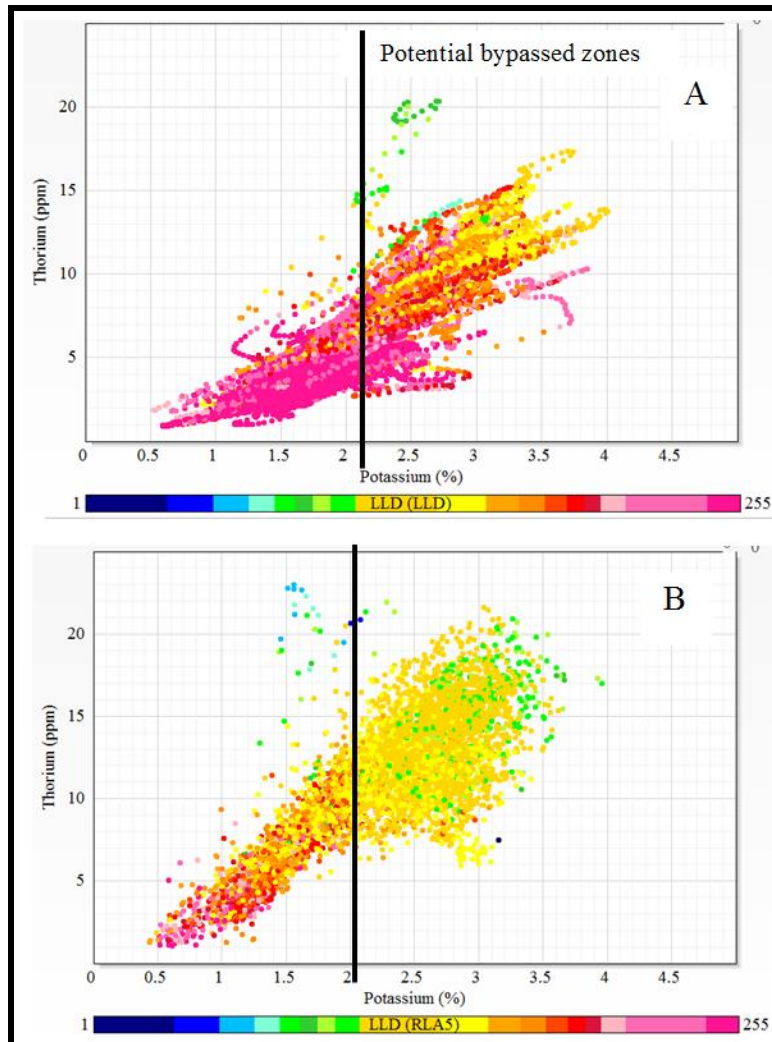


Figure 16: Thorium and potassium crossplots used to estimate the effect of clay on resistivity log. Color scale is log of deep resistivity in ohm-m from log data. Graph shows a decrease in resistivity with an increase in thorium and potassium content.

We discussed the effect of mineralogy, textural, and geological characteristics of the rock on velocity-porosity and NMR response of the Monterey samples. Three main mineral groups: quartz, carbonate, and clays have significant effects on the amplitude and location of the peaks in the NMR response of the rock. NMR  $T_2$  distributions are a representation of the pore size in the rock and are the only way to measure a downhole representation of the pore size distribution. In order to transform the  $T_2$  distributions to pore size distribution we need surface relaxivity values. In the following section we use mercury intrusion (MI) data to calculate the surface relaxivity values. Saidian et al. (2014) discussed the reliability of the NMR-MI technique for this sample set. They concluded that due to the large pore throat sizes (up to 100 nm) measured by the MI technique the comparison of NMR and MI is reliable in these samples.

#### NMR and Mercury Injection Relationship

As mentioned earlier the distributions of NMR relaxation data can be affected by the parameters used to performed the experiment and the mathematical inversion used on the amplitude data (conversion from amplitude to  $T_2$ ). In order to obtain reliable pore size distributions from  $T_2$  relaxation times, we compared our results with mercury injection results on selected samples. The mercury injection experiments for samples 5477.1 and 7751.8 were performed by an outside vendor.

This analysis is based on the principle that in a water-wet, fully water-saturated rock, the  $T_2$  relaxation time of a single pore is proportional to the surface area to volume ratio of that pore, which in turn is a measure of the size of

the pore (Marschall et al., 1995, Coates et al. 1999, and Dunn et al., 2002). Thus, PSD from NMR data can be compared to the pore throat size distribution obtained from mercury injection data. However, in order to compare the data, the pore radius data obtained from mercury injection is converted to an equivalent T<sub>2</sub> value. According to:

$$T_2 = \frac{1000r}{2\rho_e} \quad (\text{Marschall et al., 1995})$$

where  $T_2$  is in msec,  $r$  is the pore radius obtained from mercury injection in  $\mu\text{m}$ , and  $\rho_e$  is the effective surface relaxivity in  $\mu\text{m}/\text{sec}$ . Marschall et al., 1995 noted that the effective surface relaxivity term is introduced to account for the fact that NMR responds to pore body size whereas mercury injection capillary pressure is controlled by pore throat sizes. The  $\rho_e$  is proportional to the product of intrinsic surface relaxivity and ratio of pore throat size to pore body size. Figure 17 shows the relationship between mercury-injection pore size distribution and  $T_2$  distribution for sample 7751.8. Note that the mercury injection data matches NMR data for a  $\rho_e$  of 6  $\mu\text{m}/\text{s}$ . This value is in accordance to values reported by Coates et al. (1999) who obtained a value of 5.35  $\mu\text{m}/\text{s}$  for a dolomitic rock. However, sample 8539 which was mainly composed of dolomite, obtained a value of 1  $\mu\text{m}/\text{s}$ , which points out the possible effect of having a mix of mineralogy.

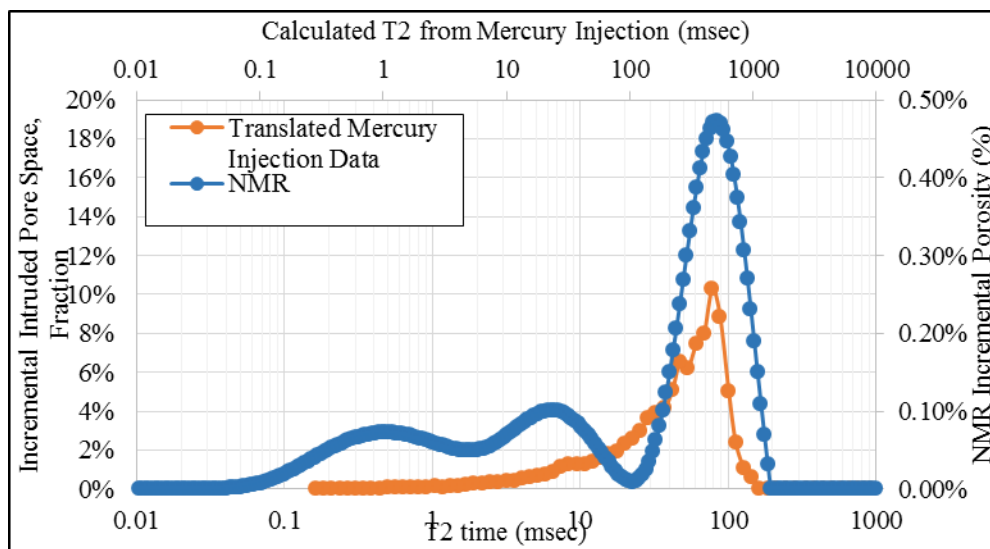


Figure 17: Relationship between mercury-injection pore size distribution and  $T_2$  distribution for sample 7751.8. The original mercury injection data was translated by using a  $\rho_e$  of 6  $\mu\text{m}/\text{sec}$ .

Table 6 provide of the summary of the parameters found through the analysis and comparison between mercury injection porosity and NMR porosity. For the most part, NMR porosity is higher than mercury injection porosity. The difference between the readings might be due to the fact that only 2 grams were used for mercury injection measurements whereas the whole core was analyzed in NMR measurements. Also, one of the main limitations of the mercury intrusion technique is the limited accessibility of the mercury to the pore space. This technique does not access the pore bodies with throats smaller than 3.6 nm (at 6000 psi mercury pressure). In samples with smaller pores there is a possibility that this technique does not measure the portion of pore space associated with smaller pores (for more information see Saidian et al., 2014). Another interesting observation is that quartz dominated samples have a  $\rho_e$  value used of 2  $\mu\text{m}/\text{s}$ . This is significantly lower than the values reported by Coates et al. (1999) who published a value of 23  $\mu\text{m}/\text{s}$  for sandstone. However, the difference between the numbers can be explained by the fact that rocks in the Monterey formation with high quartz content are not well represented by sandstones. Quartz rich rocks in the Monterey formation are marked by a considerable amount of small pore sizes, therefore the  $\rho_e$  would also be small.

Table 6: Effective surface relaxivity found for cores and mercury injection porosity.

Core	NMR Porosity (p.u.)	Effective Surface Relaxivity, $\rho_{es}$ ( $\mu\text{m}/\text{sec}$ )	Mercury Injection Porosity (p.u.)
5477.1	7	2	4.7
7228.2	6	1	3.8
7750.8	8	1	8.4
7751.8	16	6	21.9
8539	2	1	3.4
8632	3	1	2.8
8935	2	1.8	1.1
9193	4	5	0.7

## 6. Conclusions

The applications of this study for the Monterey formation can have a significant impact. The immediate and most important conclusion is that compressional velocity – porosity trends as well and NMR pore size distributions show that rocks with considerable amount of carbonate or dolomite content correlate well with oil/water ratio from dean stark experiment in cores. Additionally, this study shows that rocks from the lower section of the Monterey have different factors that make it unique when compared to upper sections that have previously been studied. Specifically:

- The lower section of the Monterey (McDonald and Devilwater) has an increasing amount of carbonate content that increases the density and velocity of rocks.
- Small pore sizes (micron range) make up a considerable amount of the porosity for biogenic quartz phase rocks in the Monterey. This points out to one of the main differences between siliceous and clastic rocks.
- The lower section of the Monterey (McDonald and Devilwater) is marked by an increasing amount of detrital clay content that is identified by an increase in thorium content. The increase in clay content increases the NPHI readings in logs and decreases the resistivity values.

Additionally, on a more practical aspect it was found that NMR measurements can provide good estimation of porosity and pore size distributions for the Monterey formation.

## 7. Acknowledgements

We would like to thank OCLASSH and Center for Rock Abuse groups for support and funding of the research. Additionally we would like to thank Benjamin Harrell his help on mercury intrusion experiments.

## 8. References

- Anderson, W.G., 1986, Wettability Literature Survey – Part 1: Rock/Oil Brine Interactions and the Effects of Core Handling on Wettability, Society of Petroleum Engineers, Journal of Petroleum Technology.
- Barron, J. A., 1986a, Paleooceanographic and tectonic controls on deposition of the Monterey Formation and related siliceous rocks in California: Paleogeography, Paleoclimatology, Paleoecology, V. 53, pp. 27 -45.
- Behl, R.J., 1999, Since Bramlette (1946): the Miocene Monterey Formation of California revisited: Geological Society of America Special Paper 338.
- Blake, M.C., Campbell, R. H., Dibblee, T.W., Howell, D. G., Nilsen, T. H., Normark, W. R., Vedder, J. C., and Silver, E. A., 1978, Neogene basin formation in relation to plate-tectonic evolution of the San Andreas Fault System, California: American Association of Petroleum Geologists Bulletin, V. 62, pp. 344-372.

- Bohacs, K.M., Grabowski, G.J., Carroll, A.R., Mankiewicz, P.J., Miskell-Gerhardt, K.J., Schwalbach, J.R., Wegner, M.B., and Simo, J.A., 2005, Production, Destruction, and Dilution – The Many Paths to Source-Rock Development, SEPM Special Publication, No. 82, pp. 61-101.
- Bohacs, K.M., Schwalbach, J.R., 1994, Natural gamma-ray spectrometry of the Monterey Formation at Naples Beach, California: insights into lithology, stratigraphy, and source-rock quality, Field Guide to the Monterey Formation between Santa Barbara and Gaviota, California: Pacific Section AAPG, V. GB72, pp.85-94.
- Coates, G.R., Xiao, L., Prammer, M.G., 1999, NMR Logging Principles and Applications, Halliburton Energy Services Publication, Houston, USA.
- Dunn, K. J., Bergman, D. J., and Latorraca, G. A., 2002, Nuclear Magnetic Resonance Petrophysical and Logging Applications, Hand book of Geophysical Exploration: Seismic Exploration, Vol. 32, Oxford, UK.
- Gassmann, F., 1951, Uber die elastizitat poroser medien: Veierteljahrsschrift der Naturforschenden Gesellschaft in Zurich, 96, pp. 1-23.
- Godinez, L., 2013, Control Factors for Fluid Saturation and Pore Size Distributions Based on Gas Adsorption, CEC, and 2D Dielectric Microscopy, Master Thesis, Golden, CO.
- Greeney, N.S., Godinez, L., 2013, Spontaneous Imbibition: Investigation of Mineral Content on Fluid Distribution in Quartz Phase Porcelanite Using Dielectric Microscopy, Golden, CO.
- Hart, B. S., Macquaker, J.H. S., Taylor, K. G., 2013, Mudstone (“shale”) depositional and diagenetic processes: Implications for seismic analyses of source-rock reservoirs. Society of Exploration Geophysicists and American Association of Petroleum Geologists.
- Hassan, M., Hossin, A & Combaz, A., 1976, Fundamentals of the differential gamma ray log interpretation technique. SPWLA 17<sup>th</sup> Annual Symposium Transactions Paper 8, pp.1-7.
- Ingle, J.C., Jr., 1981, Origin of Neogene diatomites around the north Pacific rim, in Garrison, R.E., and Douglas, R. G., eds., The Monterey Formation and related siliceous rocks of California: Los Angeles, Pacific Section, Society of Economic Paleontologists and Mineralogists, pp. 159-179.
- Isaacs, C.M., 1985, Abundance versus rates of accumulation in fine-grained strata of the Miocene Santa Barbara basin, California, Geo-Marine Letters, V. 5, pp. 25-30.
- Mavko, G., Chan, C., and Mukerji, T., 1995, Fluid substitution: Estimating changes in  $V_p$  without knowing  $V_s$ . Geophysics, V. 60, pp. 1750-1755.
- Punturo, R., Kern H., Cirrincione, R., Mazzoleni, P., Pezzino, A., 2005, P- and S-wave velocities and densities in silicate and calcite rocks from the Peloritani Mountains, Sicily (Italy): The effect of pressure, temperature, and the direction of wave propagation, Elsevier Tectonophysics, pp. 55-72.
- Schwalbach, J.R., Gordon, S.A., O'Brien, C.P., Lockman, D.F., Benmore, W.C., Huggins, C.A., 2009, Reservoir Characterization of Monterey Formation Siliceous Shales: Tools and Applications, Pacific Section AAPG Publication MP48, pp. 119-146.
- Sharma, R., Prasad, M., Batzle, M.L., Vega, S., 2013, Sensitivity of Flow and Elastic Properties to Fabric Heterogeneity in Carbonates, Geophysical Prospecting, 61, 270–286.
- Tada, R., and Lijima A., 1983, Petrology and diagenetic changes of Neogene siliceous rocks in northern Japan, Journal of Sedimentary Research, pp. 911-930.